J. Phys. D: Appl. Phys. **43** (2010) 035302 (11pp) doi:10.1088/0022-3727/43/3/035302

Experimental and computational study on the phase stability of Al-containing cubic transition metal nitrides

Florian Rovere[1,2,4], Denis Music[2], Sergey Ershov[2], Moritz to Baben[2], Hans-Gerd Fuss[3], Paul H Mayrhofer[1] and Jochen M Schneider[2]

[1] Department of Physical Metallurgy and Materials Testing, Montanuniversität Leoben, A-8700 Leoben, Austria
[2] Materials Chemistry, RWTH Aachen University, D-52056 Aachen, Germany
[3] CemeCon AG, D-52146 Würselen, Germany

E-mail: florian.rovere@mu-leoben.at

Received 4 August 2009, in final form 16 November 2009
Published 8 January 2010
Online at stacks.iop.org/JPhysD/43/035302

Abstract

The phase stability of Al-containing cubic transition metal (TM) nitrides, where Al substitutes for TM (i.e. $TM_{1-x}Al_xN$), is studied as a function of the TM valence electron concentration (VEC). X-ray diffraction and thermal analyses data of magnetron sputtered $Ti_{1-x}Al_xN$, $V_{1-x}Al_xN$ and $Cr_{1-x}Al_xN$ films indicate increasing phase stability of cubic $TM_{1-x}Al_xN$ at larger Al contents and higher temperatures with increasing TM VEC. These experimental findings can be understood based on first principle investigations of ternary cubic $TM_{1-x}Al_xN$ with TM = Sc, Ti, V, Cr, Y, Zr and Nb where the TM VEC and the lattice strain are systematically varied.

However, our experimental data indicate that, in addition to the decomposition energetics (cubic $TM_{1-x}Al_xN \rightarrow$ cubic TMN + hexagonal AlN), future stability models have to include nitrogen release as one of the mechanisms that critically determine the overall phase stability of $TM_{1-x}Al_xN$.

(Some figures in this article are in colour only in the electronic version)

1. Introduction

Al-containing face centred cubic (fcc, B1 structure) transition metal nitrides (TMN), where Al substitutes for TM (i.e. fcc-$TM_{1-x}Al_xN$), exhibit considerable improvements of mechanical and chemical properties as compared with their binary counterparts. Here, particularly $Ti_{1-x}Al_xN$ and more recently $Cr_{1-x}Al_xN$ [1–6], which can be synthesized by physical vapour deposition in their cubic metastable state, have found widespread applications as protective coatings in advanced machining [7–11], as wear and corrosion resistant coatings for different tools [12–16], or in electronic devices [17].

Based on their industrial importance many research activities focus on the synthesis, structure and properties of $TM_{1-x}Al_xN$. The metastable solubility limits of AlN in fcc-$TM_{1-x}Al_xN$ films were experimentally determined to be $x = 0.5$–0.91 for $Ti_{1-x}Al_xN$ [18–24], $x = 0.6$–0.71 for $Cr_{1-x}Al_xN$ [10, 20, 25–28], $x = 0.3$–0.43 for $Zr_{1-x}Al_xN$ [29–31] and $x = 0.5$–0.6 for $Nb_{1-x}Al_xN$ [32]. When the critical AlN contents are exceeded the hexagonal closed packed (hcp, B4) wurtzite structure crystallizes, which generally results in unfavourable coating performances [10, 29]. Detailed information on the thermal stability based on differential scanning calorimetry (DSC) investigations is mainly available for $Ti_{1-x}Al_xN$ [22, 33] and $Cr_{1-x}Al_xN$ [34–37].

Connected with the increase in computational power, only recently were in-depth first principle investigations on the phase stability of such ternary or multinary metastable materials carried out. Most of these reports are based on *ab initio* calculations [38–46], but also on band parameter methods [47] or thermodynamic modelling [48, 49]. In [45, 46], where a considerable number of different *ad hoc*

[4] Author to whom any correspondence should be addressed.

supercell arrangements were used, the Al distribution of the metal sublattice, connected with differences in the electronic structure, bond energy and configurational contribution to the total energy, is suggested to account for the experimentally observed spread in maximum Al contents for cubic $Ti_{1-x}Al_xN$ and $Cr_{1-x}Al_xN$. Alling *et al* [38, 40, 41] conducted studies for cubic $Sc_{1-x}Al_xN$, $Ti_{1-x}Al_xN$, $Cr_{1-x}Al_xN$ and $Hf_{1-x}Al_xN$ using the coherent potential approximation which allows one to accurately model disordered systems [38, 40, 41]. In these studies the presence of an electronic band structure mismatch, rather than differences in the lattice parameter, is suggested as the driving force for decomposition for cubic $Ti_{1-x}Al_xN$ and $Hf_{1-x}Al_xN$, whereas for cubic $Sc_{1-x}Al_xN$ and $Cr_{1-x}Al_xN$ mainly lattice strain is proposed to control phase stability. Makino on the other hand predicted critical contents of AlN for B1/B4 phase change in $TM_{1-x}Al_xN$ (TM = Ti, V, Cr, Zr, Nb, Hf and W) based on the calculation of band parameters which are in the range of experimentally obtained values but do not account for the spread in critical Al content reported in the literature [47]. However, although the stability of individual $TM_{1-x}Al_xN$ has been extensively studied experimentally and theoretically, the individual contributions of electronic configuration and lattice strain to phase stability remain unclear as in this regard no systematic study has been reported. Nevertheless such a systematic approach is essential for understanding and predicting phase stabilities of $TM_{1-x}Al_xN$.

Here, a comparative experimental study of three different $TM_{1-x}Al_xN$ systems with TM = Ti, V and Cr is conducted where identical deposition parameters were applied to allow comparison. The phase stabilities are assessed by the determination of maximum possible AlN contents before the B1/B4 phase change occurs and by thermal investigations using DSC together with thermogravimetric analysis (TGA). The individual contributions of electronic configuration and lattice strain to phase stabilities are discussed based on *ab initio* calculations of ternary cubic $TM_{1-x}Al_xN$ with TM variations in the valence electron concentration (VEC) and in the lattice parameter of the corresponding binary cubic TMN (TM = Sc, Ti, V, Cr, Y, Zr and Nb). The qualitative comparison of the individual phase stabilities is obtained by calculating and presenting the mixing enthalpies as a function of VEC and lattice strain.

2. Experimental details

$TM_{1-x}Al_xN$ (TM = Ti, V, Cr) thin films were synthesized in an industrial scale high vacuum system (CC800/9 ML) with a base pressure of 0.1 mPa by reactive magnetron sputtering with a target power density of 9.1 W cm^{-2}. Four rectangular targets (10 × 88 × 500 mm^3) consisting of a half of pure Ti, V or Cr and an Al half (both of triangular shape) were used to prepare compositional gradient thin films. The films were grown on low alloyed steel sheets during two-fold rotation and on cemented carbide inserts during three-fold rotation to a thickness of 4–5 μm. The minimum target–substrate distance was 50 mm. The substrates were heated to ∼450 °C and a dc bias potential of −90 V was applied. The total Ar/N_2 pressure of 580 mPa (360 sccm Ar, 100 sccm N_2) was kept constant throughout the depositions.

The film compositions were determined using energy dispersive x-ray (EDX) analyses (EDAX Genesis 2000) in a JEOL JSM 6480 scanning electron microscope (SEM). Quantification was performed by using $TM_{1-x}Al_xN$ (TM = Ti, V, Cr) standards analysed by wavelength dispersive x-ray spectroscopy.

Based on the EDX data the coated low alloyed steel substrates were cut into strips of 2 cm width associated with a compositional variation in the AlN content x of ±0.02. To avoid substrate interference during thermal and structural analyses the films were separated from the low alloyed steel substrates by dissolving the steel foil in ∼6 mol% nitric acid ($Ti_{1-x}Al_xN$ and $Cr_{1-x}Al_xN$) or in ∼6 mol% hydrochloric acid ($V_{1-x}Al_xN$). The free-standing films were subsequently ground to a powder.

The thermal stability as a function of chemical composition was investigated by simultaneous dynamic DSC and TGA in a Netzsch STA 449C Jupiter calorimeter for post-deposition annealing temperatures T_a up to 1600 °C. The measurements were carried out in flowing Ar (99.999% purity, 15 sccm flow rate) at atmospheric pressure using a heating rate of 20 °C min^{-1} and the maximum cooling rate of 50 °C min^{-1} to minimize further reactions. Structural investigations of the powdered films in the as-deposited state and after DSC measurements at 900, 1000, 1100, 1200, 1300 and 1600 °C were conducted by x-ray diffraction (XRD), using a Bruker D8 diffractometer with a SolX detector in the Bragg–Brentano configuration with Cu Kα radiation (λ = 1.540 56 nm). For the identification of individual XRD peaks, the JCPDS database was used [50].

3. Computational details

The calculations in this work were carried out using density functional theory [51], as implemented in the Vienna Ab-initio Simulation Package (VASP) [52, 53], where the projector augmented wave potentials with the generalized-gradient approximation (GGA) are employed [54]. The following parameters were applied: convergence criterion for the total energy of 0.01 meV, Blöchl corrections for the total energy [55], cut-off of 500 eV, integration in the Brillouin zone according to Monkhorst–Pack [56] with 5 × 5 × 5 irreducible k-points. The convergence tests were carried out in a previous work [46]. 2 × 2 × 1 supercells containing 32 atoms (x = 0.25, 0.50, 0.75, NaCl prototype) were relaxed with respect to atomic positions and cell volumes. Energy of formation was calculated with respect to elements.

Two types of 2 × 2 × 1 supercells were probed: *ordered* and *special quasi-random structures* (*SQS*) [57]. The ordered ($L1_O$ structure) supercell used was termed in a previous work as C#1 configuration, providing the highest number of TM–Al bonds [46]. The SQS implementation via a short range order (SRO) parameter is available within the locally self-consistent Green's function software package [58, 59]. The Warren–Cowley SRO parameter [60] within three coordination shells was used to account for randomness in the metallic sublattice.

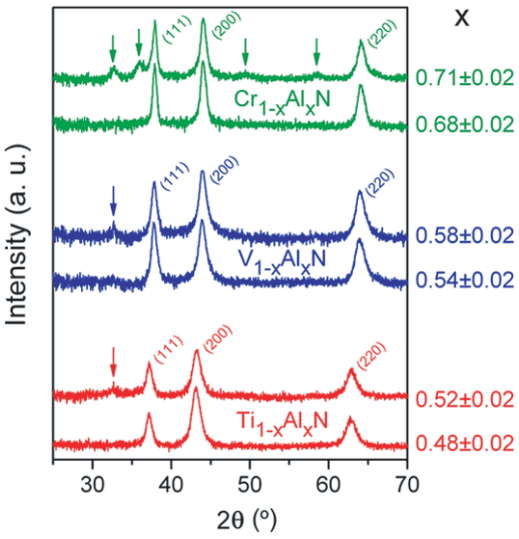

Figure 1. XRD data of magnetron sputtered $Ti_{1-x}Al_xN$, $V_{1-x}Al_xN$ and $Cr_{1-x}Al_xN$ films indicating maximum AlN (x) solubility for single phase fcc structure of $x = 0.48 \pm 0.02$, 0.54 ± 0.02 and 0.68 ± 0.02, respectively. The B4 wurtzite structure is denoted by arrows. (Colour online.)

CrN and $Cr_{1-x}Al_xN$ were calculated with antiferromagnetic (AFM) spin configuration which was realized by ferromagnetic layers with alternating spin directions for every single layer for the ordered C#1 supercell arrangements. For the SQS configuration a random spin-up–spin-down arrangement was achieved within the SQS implementation mentioned above. All other configurations were not spin polarized.

4. Results and discussion

4.1. Structural and thermal analysis

Due to the deposition technique where segmented TM–Al (TM = Ti, V, Cr) targets are used, compositional gradients in x of 0.25–0.85, 0.2–0.85 and 0.15–0.7 are obtained for $Ti_{1-x}Al_xN$, $V_{1-x}Al_xN$ and $Cr_{1-x}Al_xN$, respectively, as determined by EDX analysis. The N contents in all coatings were measured to be 52 ± 1 at% suggesting slightly overstoichiometric films. It is noteworthy that the determination of N contents by EDX analysis may not be accurate but is useful for comparison between the films investigated.

Based on XRD analysis maximum AlN contents of $x = 0.48 \pm 0.02$, 0.54 ± 0.02 and 0.68 ± 0.02 are obtained for the applied deposition parameters before the B1/B4 phase change occurs, see figure 1. Hence, $TM_{1-x}Al_xN$ (TM = Ti, V, Cr) film compositions close to $x = 0.5$ were chosen for further structural and thermal investigations. Based on the EDX data, a compositional variation of $x = 0.48 \pm 0.02$, 0.49 ± 0.02 and 0.48 ± 0.02 is present for $Ti_{1-x}Al_xN$, $V_{1-x}Al_xN$ and $Cr_{1-x}Al_xN$, respectively. To improve readability these films are referred to as $Ti_{0.5}Al_{0.5}N$, $V_{0.5}Al_{0.5}N$ and $Cr_{0.5}Al_{0.5}N$ throughout the paper.

XRD investigations indicate a single phase fcc structure with lattice parameters a of 4.19 Å, 4.12 Å and 4.13 Å and crystallite domain sizes of ∼9 nm, 15 nm and 25 nm for these $Ti_{0.5}Al_{0.5}N$, $V_{0.5}Al_{0.5}N$ and $Cr_{0.5}Al_{0.5}N$ films, respectively, as obtained by the pseudo-Voigt single line method [61] evaluating the (1 1 1) diffraction peak. Since identical deposition conditions were employed for all the films, the increasing crystallite domain size from ∼9 nm to 15 nm to 25 nm for $Ti_{0.5}Al_{0.5}N$, $V_{0.5}Al_{0.5}N$ and $Cr_{0.5}Al_{0.5}N$, respectively, may be associated with increasing adatom mobilities. A constant deposition temperature of ∼450 °C results in increasing homologous temperatures from ∼0.2 to 0.24 to 0.55 for $Ti_{1-x}Al_xN$, $V_{1-x}Al_xN$ and $Cr_{1-x}Al_xN$, respectively, as the decomposition temperatures of the binary constituents decrease from 3290 °C at 10^5 Pa for TiN to 2100 °C at 10^5 Pa for VN to 1050 °C at 10^5 Pa for CrN [62, 63]. This is consistent with the cross sectional SEM investigations of these coatings on cemented carbide substrates. The column width clearly increases from $Ti_{0.5}Al_{0.5}N$ to $V_{0.5}Al_{0.5}N$ to $Cr_{0.5}Al_{0.5}N$, see figures 2(*a*)–(*c*).

Figure 3 presents simultaneous thermal analysis data for the $TM_{0.5}Al_{0.5}N$ (TM = Ti, V, Cr) films considered here. Identification of the major features in the DSC (figure 3(*a*)) and TGA (figure 3(*b*)) signals of $Ti_{0.5}Al_{0.5}N$, $V_{0.5}Al_{0.5}N$ and $Cr_{0.5}Al_{0.5}N$ is achieved by XRD analyses after DSC investigations at the temperatures of interest, see figures 4(*a*), (*b*) and (*c*), respectively.

Although there are many overlapping exothermic and endothermic reactions during annealing of these metastable coatings to 1600 °C we will focus only on the main features detected during the DSC–TGA measurements. The first exothermic main contribution to the DSC signals during heating is observed for all the films at ∼500 °C, see figure 3(*a*). These exothermic features (indicated in figure 3 with A^1, A^2 and A^3) can be related to relaxation and recovery processes of point, line and area defects as the annealing temperature exceeds the deposition temperature [64].

The XRD investigations for $T_a = 900$ °C (∼ the peak temperature for B^1 in figure 3(*a*)), see figure 4(*a*), indicate decomposition of the metastable fcc-$Ti_{0.5}Al_{0.5}N$ matrix to form cubic TiN- and AlN-rich domains and also hcp-AlN. As has been reported before, the formation of cubic TiN- and AlN-rich domains is related to spinodal decomposition before nucleation and growth processes of hcp-AlN occur [19, 43, 44, 64–66]. The XRD peak width of the cubic phases for $T_a = 900$ °C is increased as compared with the as-deposited state and particularly on the left side of the matrix peaks the formation of a shoulder, indicating TiN-rich domains, can be observed. As the temperature is increased to 1000 °C the width of the XRD peaks of the cubic phases increases further and also the peak maximum shifts to lower diffraction angles indicating the continued decomposition of the cubic $Ti_{1-x}Al_xN$ matrix towards fcc-TiN, fcc-AlN and hcp-AlN. This is consistent with the formation of a shoulder on the high angle side of the cubic matrix peaks.

The TGA data, figure 3(*b*), indicate that the mass continuously decreases with increasing temperature reading a value of ∼0.34 wt% at 950 °C. A further increase in temperature to 1200 °C results in a pronounced mass loss of ∼2.76 wt% corresponding to ∼5.1 at% in N. For temperatures above 1200 °C only a minute mass loss is observed. In

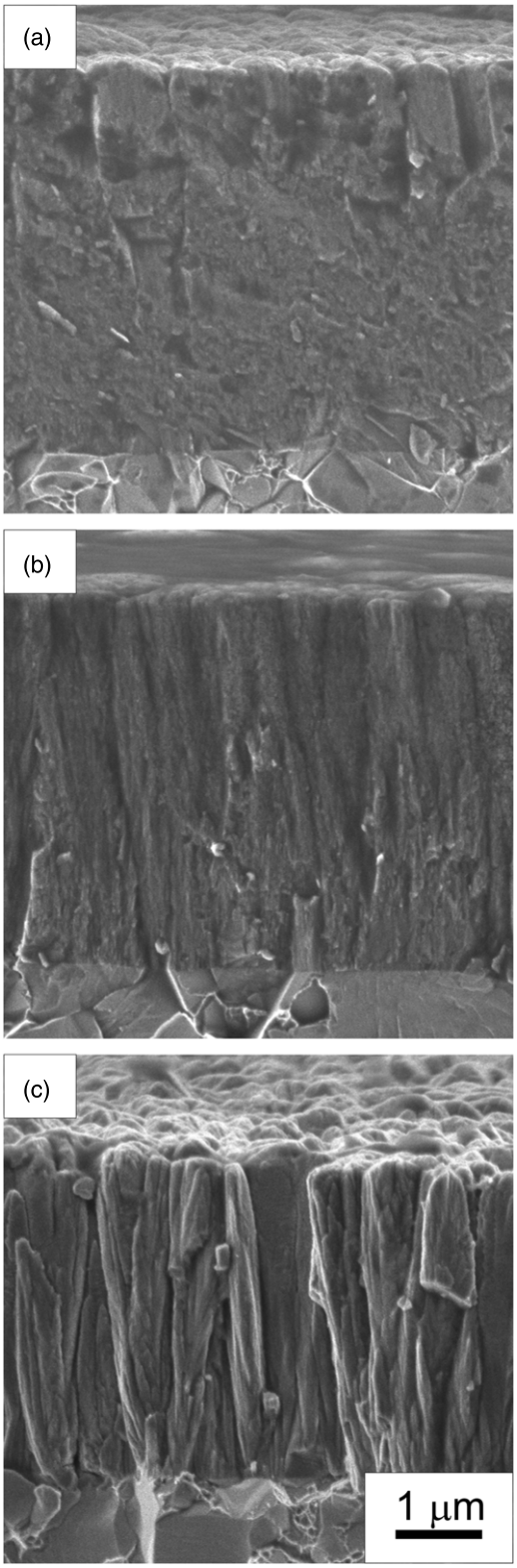

Figure 2. Cross sectional SEM images of (*a*) $Ti_{0.5}Al_{0.5}N$, (*b*) $V_{0.5}Al_{0.5}N$ and (*c*) $Cr_{0.5}Al_{0.5}N$ on cemented carbide substrates.

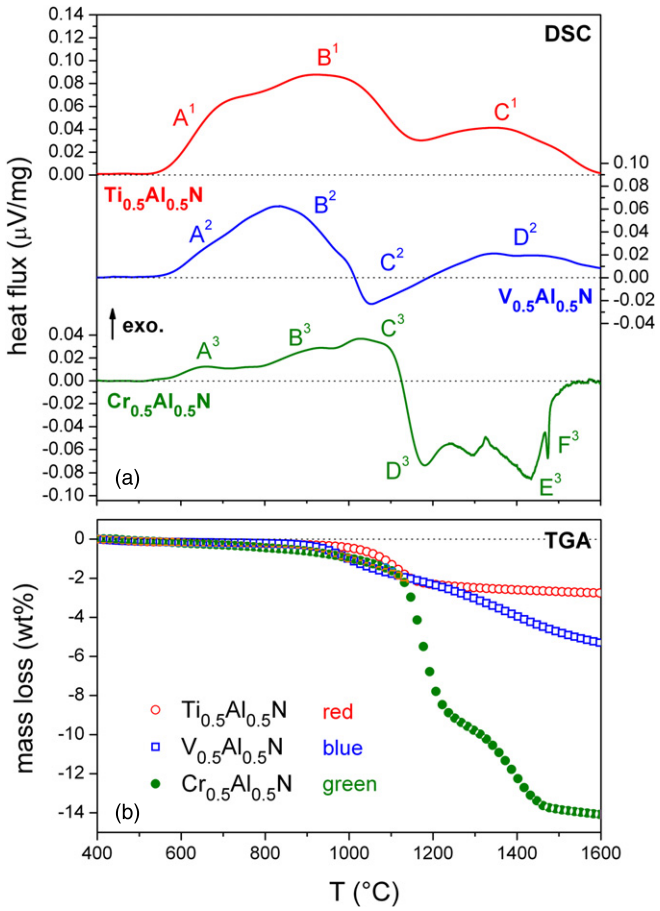

Figure 3. Dynamical, simultaneous thermal analysis in inert atmosphere (Ar) combining (*a*) DSC and (*b*) thermogravimetry of cubic $Ti_{0.5}Al_{0.5}N$ (red), $V_{0.5}Al_{0.5}N$ (blue) and $Cr_{0.5}Al_{0.5}N$ (green). (Colour online.)

agreement with previous reports the mass loss can be associated with N release [33]. Based on XRD data, see figure 4(*a*), the N release is connected with the formation of hcp-AlN from the parent cubic matrix or any previously formed fcc-AlN. As the $Ti_{1-x}Al_xN$ coatings considered here exhibit an over-stoichiometry of maximum 3 at% we propose that N is also released by other mechanisms during fcc → hcp-AlN phase transformation or during nucleation and growth of hcp-AlN.

In the temperature range 1200–1600 °C a third major exothermic contribution (C^1) can be detected during DSC, see figure 3(*a*). The corresponding XRD analyses, see figure 4(*a*), indicate fcc → hcp-AlN transformation, grain growth and recrystallization processes to be responsible for this DSC feature. After completed decomposition of the metastable cubic $Ti_{0.5}Al_{0.5}N$ phase, the XRD peaks for fcc-TiN are almost at the corresponding JCPDS reference positions [50]. The XRD peak positions for hcp-AlN on the other hand are slightly shifted to higher 2θ angles as compared with their standard positions indicating a smaller lattice parameter which may be due to N deficiency and/or remaining stresses.

The dominant features in the DSC signal of $V_{0.5}Al_{0.5}N$ are the previously mentioned exothermic relaxation and recovery processes A^2 in the temperature range $500 < T < 1200$ °C, a subsequent further exothermic contribution B^2 for $800 < T < 1000$ °C, an overlapping endothermic part C^2 with $900 < T < 1200$ °C and a concluding exothermic contribution D^2 for $T > 1200$ °C, see figure 3(*a*).

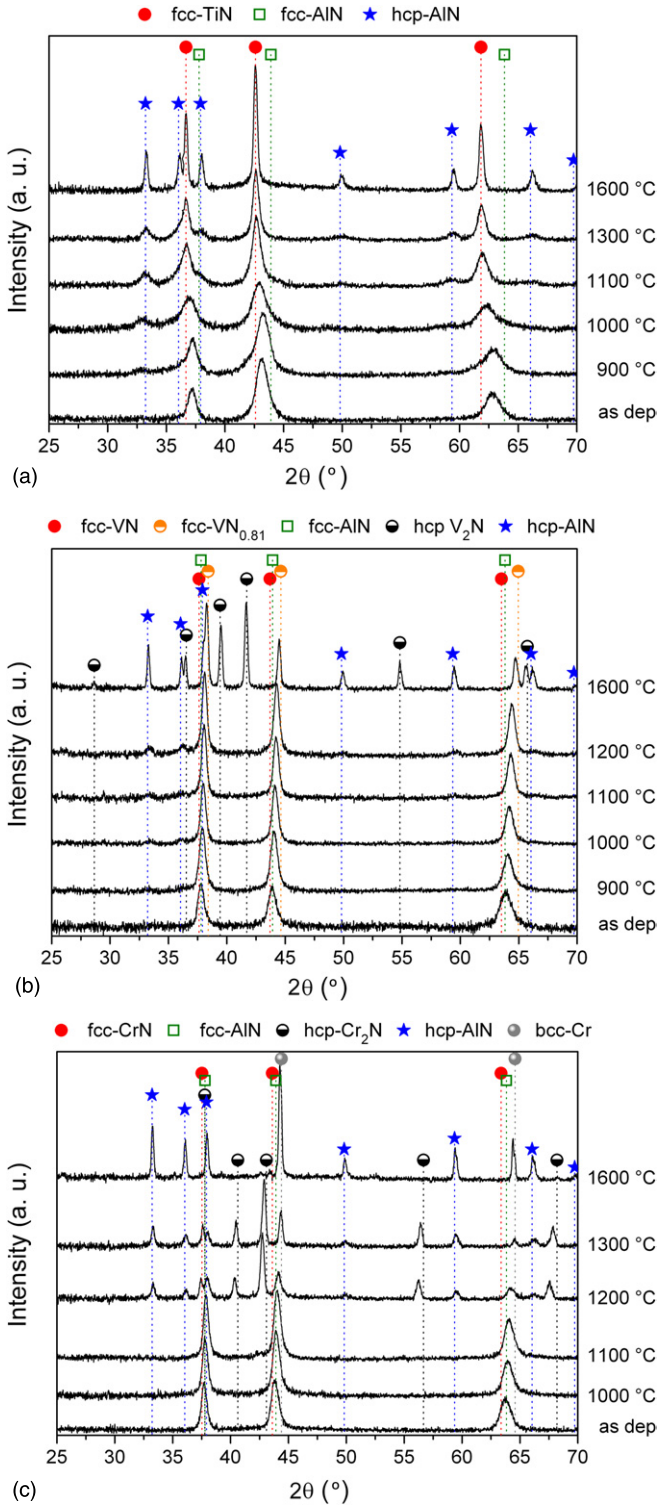

Figure 4. XRD powder scans of cubic (*a*) $Ti_{0.5}Al_{0.5}N$, (*b*) $V_{0.5}Al_{0.5}N$ and (*c*) $Cr_{0.5}Al_{0.5}N$ at the as-deposited state and after annealing up to 1600 °C. (Colour online.)

The corresponding XRD data, see figure 4(*b*), indicate that no fcc-AlN is present for any T_a and also no increase in the width of the cubic matrix peaks with T_a occurs (in contrast to $Ti_{1-x}Al_xN$). This is consistent with the notion of nucleation and growth controlled film decomposition rather than spinodal decomposition. As indicated by lower hcp-AlN peak intensities, considerably less hcp-AlN is present for $T_a = 900$ °C as compared with $Ti_{0.5}Al_{0.5}N$, see figures 4(*a*) and (*b*). Furthermore, a notably smaller increase in peak intensity with temperature suggests a less rapid decomposition of $V_{0.5}Al_{0.5}N$ as compared with $Ti_{0.5}Al_{0.5}N$.

For $V_{0.5}Al_{0.5}N$ a continuous mass loss, related to the release of over-stoichiometric N in agreement with $Ti_{0.5}Al_{0.5}N$, is observed with increasing temperature from 500 to 900 °C. At higher temperatures a two-stage mass loss occurs resulting in a total mass deficit of 5.31 wt% corresponding to 10.1 at% N for $V_{0.5}Al_{0.5}N$. After annealing to 1600 °C, the phases hcp-AlN and hcp-V_2N together with a N-deficient VN (corresponding to fcc-$VN_{0.81}$) can be detected. Consequently, the endothermic feature during DSC, labelled C^2 in figure 3(*a*), is attributed to N release connected with the dissociation of V–N bonds. Thereby, in contrast to $Ti_{0.5}Al_{0.5}N$, the lattice parameter of the residual $V_{1-x}Al_xN$ matrix decreases with increasing temperature, as indicated by increasing XRD angles, see figure 4(*b*). The dissociation of V–N bonds is triggered by the precipitation of hcp-AlN, which is connected with a reduction in the Al content in the remaining matrix and hence a reduction in phase stability as observed for $Cr_{1-x}Al_xN$ [34, 37, 67]. According to the calculated phase diagrams for the nitrogen–vanadium system [63, 68], VN starts to gradually release N connected with the formation of VN_{1-x} at above ~900 °C for 100 kPa, before the spontaneous $VN_{1-x} \rightarrow V_2N$ transformation occurs at ~2100 °C. The gradual N release is accompanied by a decreasing lattice parameter which is consistent with our observations, see figure 4(*b*). As obtained by the XRD analysis, V_2N can be detected already at 1600 °C which is considerably below the calculated temperature of ~2100 °C [63, 68]. This may be explained by a strong dependence of the dissociation of V–N bonds on the N partial pressure, which is low during our DSC investigations in Ar atmosphere. The N partial pressure was shown to have a significant effect on the onset of decomposition induced N loss for $Cr_{1-x}Al_xN$ [34]. For temperatures above 1200 °C nucleation and growth processes of hcp-AlN in addition to recrystallization processes (as obtained from the XRD data as a function of temperature, figure 4(*b*)) offset the endothermic contribution of V–N dissociation and result in an overall exothermic contribution to the DSC signal indicated by D^2 in figure 3(*a*).

For $Cr_{0.5}Al_{0.5}N$, the XRD analysis indicates only minute structural changes and a slightly decreasing lattice parameter on increasing the temperature to 1000 °C, see figure 4(*c*). Hence, the exothermic contributions to the DSC signal, indicated by A^3 and B^3 in figure 3(*a*), can be attributed to processes involving recovery, relaxation and onset of recrystallization in agreement with earlier studies [35, 36].

As for $Ti_{1-x}Al_xN$ and $V_{1-x}Al_xN$, also for $Cr_{1-x}Al_xN$ a continuous mass loss due to the release of over-stoichiometric N is detected from 500 to 900 °C. In fact the N concentrations of 52 ± 1 at% for all three ternaries considered here yield comparable mass losses for $T \leqslant 900$ °C. For a further increase in temperature (>1000 °C) the onset of a two-stage enhanced mass loss connected with decomposition induced N release is

observed (fcc $-$ $Cr_{1-x}Al_xN$ $\rightarrow$ hcp $-$ AlN + hcp $-$ Cr_2N + N_2 $\rightarrow$ hcp $-$ AlN+bcc $-$ Cr + N_2 [36, 37]), see figure 3(*b*), where dissociation of Cr–N bonds is promoted when nucleation and growth processes of hcp-AlN result in a gradually Cr-enriched remaining matrix. The XRD data indicate the presence of hcp-AlN and hcp-Cr_2N together with retained $Cr_{1-x}Al_xN_{1-y}$ at 1200 °C, see figure 4(*c*). Consequently, the exothermic feature C^3 which is superimposed by the endothermic contributions D^3 and E^3, associated with Cr–N decomposition (fcc-CrN $\rightarrow$ hcp-Cr_2N + N_2 $\rightarrow$ bcc-Cr + N_2), is attributed to nucleation and growth of hcp-AlN and recrystallization processes, compare figures 3(*a*) and 4(*c*). Also for $Cr_{0.5}Al_{0.5}N$ no broadening of the respective XRD peaks can be detected with increasing temperature indicating no fcc-AlN formation. Hence, the film decomposition is controlled by nucleation and growth processes of hcp-AlN without spinodal decomposition. The small, endothermic contribution to the DSC signal at ~1473 °C (F^3) is associated with the melting of impurity Fe-based particles which could not be removed during substrate dissolution. This is consistent with a corresponding small endothermic contribution at ~1536 °C (not shown here) when the samples are measured again and the Fe particle size dependent melting point reduction disappears due to agglomeration [69]. The corresponding Fe volume fraction in the measured powders is below the ~2% detection limit of XRD.

After annealing to 1600 °C, the XRD data show only hcp-AlN and bcc-Cr indicating a total decomposition of $Cr_{1-x}Al_xN$ into its stable constituents involving a complete dissociation of Cr–N bonds, see figure 4(*c*).

The measured total mass loss of 14.1 wt%, see figure 3(*b*), is in excellent agreement with a theoretical mass loss of 14.2 ± 0.28 wt% (27 ± 2 at% N) when all Cr-bound N is released from $Cr_{0.25\pm0.02}Al_{0.24\pm0.02}N_{0.52\pm0.01}$ ($Cr_{0.5}Al_{0.5}N$).

If the annealing temperature, where hcp-AlN can be detected for the first time, is considered as the onset of decomposition, $Cr_{0.5}Al_{0.5}N$ exhibits a significantly higher onset temperature as compared with $Ti_{0.5}Al_{0.5}N$ and $V_{0.5}Al_{0.5}N$. The XRD analysis after annealing to 1000 °C clearly reveals hcp-AlN for $Ti_{0.5}Al_{0.5}N$ and $V_{0.5}Al_{0.5}N$ but only minute structural changes are observed for $Cr_{05}Al_{0.5}N$, compare figures 4(*a*)–(*c*). These data suggest a decreasing driving force for the decomposition from $Ti_{1-x}Al_xN$ to $V_{1-x}Al_xN$ to $Cr_{1-x}Al_xN$. This is consistent with the observed increasing attainable maximum Al contents of $x = 0.48\pm0.02$, 0.54 ± 0.02 and 0.68 ± 0.02 for $Ti_{1-x}Al_xN$, $V_{1-x}Al_xN$ and $Cr_{1-x}Al_xN$, respectively, compare figure 1.

However, as soon as the decomposition of the metastable cubic $TM_{1-x}Al_xN$ (TM = Ti, V, Cr) matrix occurs and hcp-AlN is formed, the remaining matrix becomes depleted in Al and changes towards fcc-TMN (TM = Ti, V, Cr). Whereas fcc-TiN is thermally stable in the temperature range investigated, fcc-VN partly dissolves to form fcc-VN_{1-x} ($VN_{0.81}$) and hcp-V_2N, and fcc-CrN completely dissociates into bcc-Cr and N_2 when the temperature is increased to 1600 °C. This is in agreement with the considerably different thermal stabilities of 3290 °C, 2800 °C and 1050 °C for fcc-TiN, fcc-VN and fcc-CrN, respectively [62, 63].

Table 1. Calculated energies of formation E_f and equilibrium lattice parameters $a_{0,calc}$ together with experimental values of equilibrium lattice parameters $a_{0,exp}$ and decomposition temperatures T_{dec} of different binary cubic TM (TM = Sc, Ti, V, Cr, Y, Zr and Nb). Note that for AlN the decomposition temperature of the hcp structure is given.

TMN	E_f (eV/atom)	$a_{0,calc}$ (Å)	$a_{0,exp}$ (Å) [50]	T_{dec} (°C) [70–72]
ScN	−2.985	4.496	4.500	Unknown
TiN	−2.704	4.256	4.240	3290
VN	−1.980	4.121	4.139	2100
CrN	−1.413	4.135	4.149	1050
YN	−2.742	4.917	4.894	2674
ZrN	−2.751	4.610	4.574	3410
NbN	−1.990	4.427	4.440	1370
AlN	−2.283	4.069	4.045	2800

In the following these experimental findings are discussed based on complementary first principle investigations of ternary cubic $TM_{1-x}Al_xN$ compounds with TM = Sc, Ti, V, Cr, Y, Zr and Nb.

4.2. *Computational analysis*

Table 1 summarizes the calculated energy of formation (E_f) values, as obtained from the equilibrium total energy difference between the calculated phases and the respective elements in their equilibrium crystal structure, as well as calculated and experimental equilibrium lattice parameters (a_0) for the considered cubic TMN (TM = Sc, Ti, V, Cr, Y, Zr, Nb) and cubic AlN. Furthermore, the decomposition temperatures [70–72] are given as a measure for the compound stability. The GGA based E_f values for the cubic TMN are in reasonable agreement with published values based on the local density approximation (LDA) [42]. Generally, a decreasing stability with increasing TM VEC is obtained. Considering the computational precision the energy of formation data for YN and ZrN cannot be distinguished. The overall decreasing stability with increasing VEC is associated with the population of energetically unfavourable states as soon as the six bonding states of the hybridized nonmetal p, metal s and metal d states (sp^3d^2 hybridization) are occupied which is the case already for ScN and YN where two s electrons and one d electron of Sc or Y together with three p electrons of N occupy the band [73, 74]. Hence, for larger TM VEC nonbonding and antibonding d states become populated. As for cubic TMN nonbonding and antibonding states overlap [73, 75] and their occupation is therefore not unambiguously distinguishable; these states will in the following be referred to as nonbonding states in agreement with other authors [41]. The destabilizing effect of populated nonbonding states is reflected in decreasing T_{dec} with increasing TM VEC, see table 1.

The calculated lattice parameters deviate by less than 0.8% from the reported experimental values [50] and reproduce the experimentally observed slightly larger lattice parameter of CrN (4.149 Å [50]) as compared with VN (4.139 Å [50]) which is not the case in earlier studies [42]. This is attributed to the fact that only recently was the need to account for an adequate description of the magnetic configuration of CrN

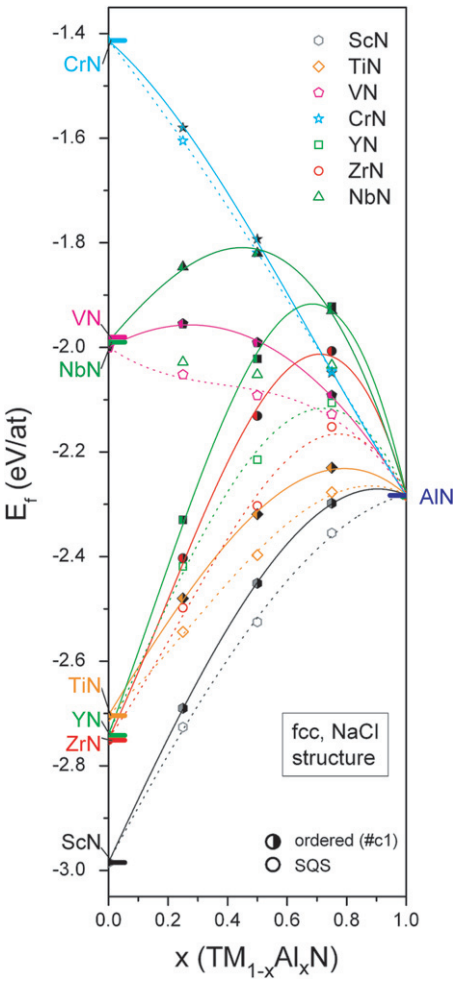

Figure 5. The energy of formation E_f for cubic ternary TM nitrides $TM_{1-x}Al_xN$ (TM = Sc, Ti, V, Cr, Y, Zr and Nb) as a function of the Al content x in ordered (C#1, filled symbols) and special quasi-random (SQS) configurations. (Colour online.)

demonstrated [40, 45] which results in larger lattice parameters and lower energies. Furthermore, it was shown that there is no significant difference in the lattice parameter, magnetization energy and energy of formation between the AFM low temperature modification, where next nearest neighbour spins are oriented antiparallel to one another (below the Néel temperature T_N (273–283 K) [76–78]), and a configuration where disordered local moments (DLM) are used to describe properly a paramagnetic high temperature modification with random-like spin polarization [40, 45]. Here, the AFM spin configuration was chosen to account for the magnetic configuration of CrN.

Figure 5 shows the calculated E_f values for the binary cubic TMN considered and cubic AlN together with values for ternary cubic $TM_{1-x}Al_xN$ ($x = 0.25$, 0.5 and 0.75) with different supercell arrangements (C#1 ordered and SQS) where third-order polynomials serve as guidelines for the eye. It can be seen that the SQS configuration yields considerably lower deviations from the mechanical mixture (the line connecting TMN and AlN), corresponding to lower ΔE_f values. This is attributed to the fact that the ordered C#1 structure represents the configuration with the highest possible number of TM(N)–Al(N) bonds. While such a highly ordered, periodic metal sublattice population is certainly not expected to form during the vapour phase condensation of a system characterized by an endothermic mixing enthalpy, it nevertheless provides valuable information on the effect of different TMs as no TM-specific structural relaxation occurs due to this high symmetry. Furthermore, as ΔE_f corresponds to the mixing enthalpy ΔH_m, the ordered C#1 configuration represents the structural configuration with the maximum possible driving force for decomposition. Figures 6(*a*) and (*b*) show the mixing enthalpies ΔH_m for cubic $TM_{1-x}Al_xN$ as a function of the Al content x calculated after

$$\Delta E_f(x) = \Delta H_m(x) = E_{f,\text{fcc}-TM_{1-x}Al_xN} - \left[(1-x)E_{f,\text{fcc}-TMN} + xE_{f,\text{fcc}-AlN}\right] \quad (1)$$

for the ordered, and the SQS configurations, respectively. $E_{f,\text{fcc-}TM_{1-x}Al_xN}$, $E_{f,\text{fcc-TMN}}$ and $E_{f,\text{fcc-AlN}}$ denote the energies of formation of fcc-$TM_{1-x}Al_xN$, fcc-TMN and fcc-AlN, respectively. It is noteworthy that the AlN-rich cubic $TM_{1-x}Al_xN$ ($x = 0.75$) yield larger mixing enthalpies as compared with the corresponding TMN-rich sides ($x = 0.25$), with $Cr_{1-x}Al_xN$ being an exception, see figure 6(*a*). This asymmetric behaviour may be explained by the fact that at high AlN contents the hybridization of TM d, TM s and N p orbitals is weakened as less TM d electrons are available to maintain the sp^3d^2 hybridization. As the hybridization is severed, the d electrons are localized at TM sites resulting in an increase in total energy. Moreover, certainly also the lack of next-nearest neighbour TM–TM bonds (weakening d–d hybridization) does account for the localization of d electrons at TM sites [41]. However, it was shown in [38–40] that such a localization of d electrons at TM sites is particularly energetically unfavourable when nonbonding states are occupied and the Fermi level E_F is forced above the minimum of the pseudogap situated between the bonding and nonbonding states. This is the case for all cubic $TM_{1-x}Al_xN$ where the TM provides more than one d electron. When the Al content for such $TM_{1-x}Al_xN$ is increased, the narrowing of the nonbonding TM d state leads to an increased DOS at the Fermi level which is known to be a destabilizing factor [79]. For $Cr_{1-x}Al_xN$ however, the negative effect of localized nonbonding TM d electrons is counteracted by magnetic effects as spin polarization of spin-up and spin-down states leads to a decrease in energy as thereby E_F falls at the valley in between nonbonding spin-up and spin-down states yielding a negligible DOS at E_F [40]. In the case of the ordered C#1 structure, the loss of hybridization and a consequently enhanced spin polarization connected with the localization of nonbonding d states at Cr sites may account for a lower ΔH_m at $x = 0.75$ as compared with $x = 0.25$, see figure 6(*a*).

Figure 6(*b*) shows the calculated ΔH_m values for the SQS configuration where again third-order polynomial fits serve as guidelines for the eye. While the number of calculated ΔH_m values is too low to allow for quantitative conclusions, it nevertheless serves as a meaningful qualitative assessment of driving forces for decomposition of random cubic $TM_{1-x}Al_xN$ with TM = Sc, Ti, V, Cr, Y, Zr and Nb. This is supported by the excellent agreement of calculated mixing

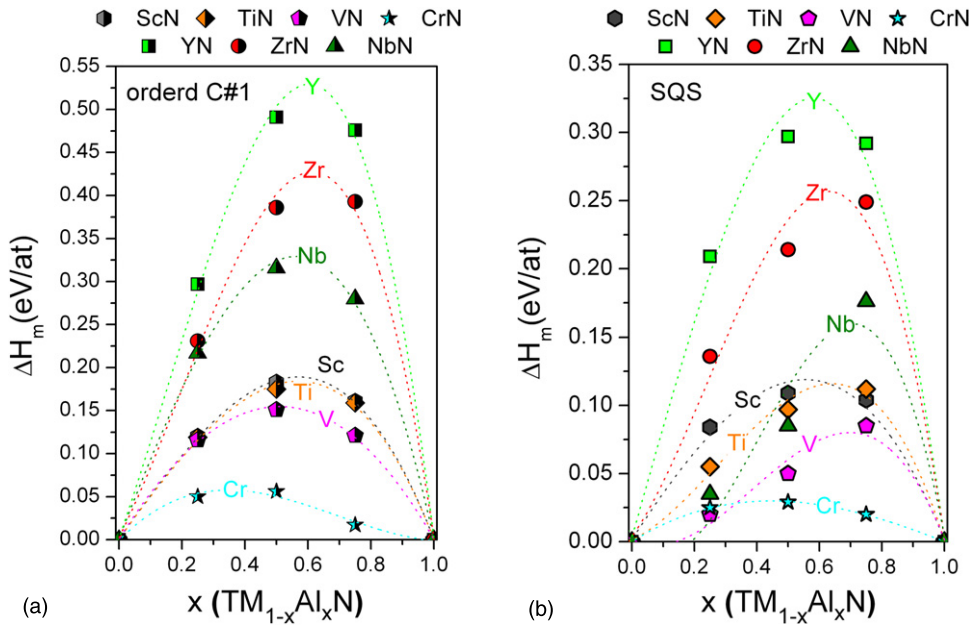

Figure 6. Mixing enthalpies H_m as a function of the Al content x for different cubic $TM_{1-x}Al_xN$ (TM = Sc, Ti, V, Cr, Y, Zr and Nb) as obtained for supercells in (*a*) ordered C#1 and (*b*) special quasi-random (SQS) configurations. (Colour online.)

enthalpies for cubic $Sc_{1-x}Al_xN$, $Ti_{1-x}Al_xN$, $Cr_{1-x}Al_xN$ and $Nb_{1-x}Al_xN$ with mixing enthalpies in other works where either a large number of different *ad hoc* supercells [46], special SQS [80] or the coherent potential approximation [38] were used to account for randomness. It is noteworthy, however, that a recently published *ab initio* study on the phase stability of $Zr_{1-x}Al_xN$ [48] suggests a considerably larger maximum mixing enthalpy of ∼80 kJ mol^{-1}, corresponding to ∼0.4 eV/atom, as compared with the obtained values of ∼0.25 eV/atom here. This might be due to the SQS formalism adopted here. At any rate, the deviation from Vegard's law in [48] is consistently larger by a factor of 1.6–1.9 as compared with this work. Also for the SQS configuration asymmetric mixing enthalpies with an increasing asymmetry for increasing TM VEC are observed. As discussed above, this is connected with the localization of d electrons at TM sites when the sp^3d^2 hybridization and the d–d hybridization weaken. $Cr_{1-x}Al_xN$ is again an exception as for the above-mentioned magnetic reasons a more symmetric mixing enthalpy is obtained, see figure 6(*b*). Based on the obtained mixing enthalpies, the tendency for decomposition for cubic $TM_{1-x}Al_xN$ decreases following the sequence TM = Y, Zr, Nb, Sc, Ti, V and Cr, compare figures 6(*a*) and (*b*).

When the calculated mixing enthalpies ΔH_m for the SQS supercell configuration are plotted against the deviation from Vegard's law [81] Δa_V, i.e. the deviation of the calculated lattice parameters from the linear relation between the lattice parameter and the concentration of the binary constituents, a linear trend with positive slope is obtained, see figure 7(*a*). Consequently, usually easily accessible lattice parameter data provide a convenient possibility to assess the mixing enthalpies and may hence serve as an indicator for the phase stability of cubic $TM_{1-x}Al_xN$. It is generally accepted that a deviation from Vegard's law occurs when electronic structure related repulsive or attractive forces between the pure constituents are present, but it was shown that it also occurs for ideal solutions when the difference in lattice parameters between the constituents exceeds 5% [82].

When the calculated mixing enthalpies ΔH_m for the SQS supercell configuration are plotted against ε, which can be considered as a qualitative measure of the strain due to the different lattice parameters of the binary constituents after [43]

$$\varepsilon = (1 - x) \cdot |\delta_{TMN}| + x \cdot |\delta_{AlN}| \tag{2}$$

with

$$\delta_{TMN} = \frac{a_V - a_{TMN}}{a_V} \quad \text{and} \quad \delta_{AlN} = \frac{a_V - a_{AlN}}{a_V}, \tag{3}$$

where a_V, a_{TMN} and a_{AlN} denote the lattice parameters for fcc-$TM_{1-x}Al_xN$ as obtained by Vegard's law, for fcc-TMN and for fcc-AlN, respectively, then within the different chemical compositions considered here (x = 0.25, 0.5 and 0.75) also linear trends are obtained, see figure 7(*b*). This presentation suggests lattice strain to be an important contribution to the phase stability of cubic $TM_{1-x}Al_xN$.

To resolve the contribution of localized d states at TM sites to phase stability for every TM considered here, a further supercell arrangement was investigated where one TM atom replaces one Al atom in a $2 \times 2 \times 1$ fcc-AlN supercell equivalent to $TM_{0.0625}Al_{0.9375}N$. This approach was chosen to allow for a meaningful comparison of the local DOS as a measure for the electronic structure related repulsive forces between TM(N) and Al(N) as the VEC is varied. The local DOS at the Fermi level are summarized in table 2. For TM = Sc, Y and Cr local DOS of zero are obtained as the Fermi level falls at the pseudogap of bonding and nonbonding states for TM = Sc and Y or in between nonbonding spin-up and spin-down states for TM = Cr, in agreement with other authors [38]. Consequently, for these TMs the localized nonbonding

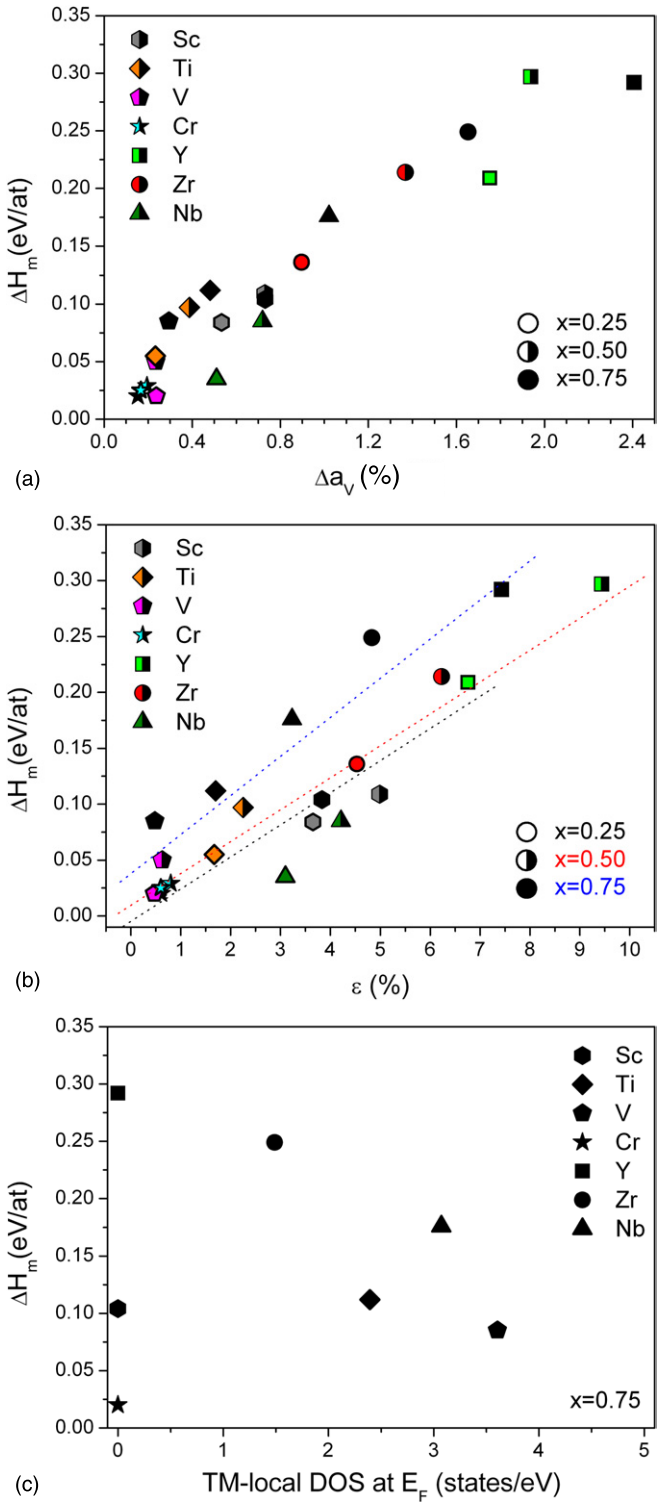

Figure 7. Calculated mixing enthalpies ΔH_m for $TM_{1-x}Al_xN$ (TM = Sc, Ti, Cr, V, Y, Zr, Nb) in the SQS supercell configuration as a function of the lattice parameter deviation from the Vegards law Δa_V (*a*), of the lattice strain ε for $x = 0.25$, 0.50 and 0.75 (*b*), and of the local DOS at E_F for $x = 0.75$ (*c*). (Colour online.)

d states do not contribute to bonding. For TM = Ti, V, Zr and Nb on the other hand, high DOS at E_F suggest an increasing destabilizing effect due to localized d electrons with increasing valency of the TM. However, when the mixing enthalpies obtained for the SQS super cell configuration at $x = 0.75$ (figure 6(*b*)), where d states become localized at TM sites (as discussed above), are plotted (see figure 7(*c*)) against the local DOS obtained for $TM_{0.0625}Al_{0.9375}N$ as a qualitative measure for the repulsive forces related to this localized d states, a negative correlation is obtained for the period-5 TM (Y, Zr, Nb) considered here. This is consistent with decreasing lattice parameters of the corresponding $TM_{1-x}Al_xN$ with increasing TM VEC and hence with the argument of lattice strain as an important contribution to phase stability. The smaller period-4 TMs (Sc, Ti, V, Cr) considered here do not exhibit a clear trend but the corresponding $TM_{1-x}Al_xN$ throughout yield smaller ΔH_m values as compared with the larger period-5 $TM_{1-x}Al_xN$.

The largest electronic driving force for decomposition, i.e. the largest DOS at E_F, is obtained for $V_{1-x}Al_xN$ where due to a low lattice strain contribution (maximum strain $\varepsilon_{0.5}$ ($x = 0.5$) of 0.6%), nevertheless, a larger phase stability is observed as compared with the other $TM_{1-x}Al_xN$ considered except for $Cr_{1-x}Al_xN$. The latter exhibits the smallest ΔH_m although the lattice strain ($\varepsilon_{0.5} = 0.8\%$) is slightly larger as compared with $V_{1-x}Al_xN$, see figure 7(*b*). This can in turn be explained by electronic effects as the Fermi level for $Cr_{1-x}Al_xN$ is unoccupied whereas it is occupied for $V_{1-x}Al_xN$ as discussed before, compare table 2. Similarly, the almost equal mixing enthalpies of $Sc_{1-x}Al_xN$ ($\varepsilon_{0.5} = 5.0\%$) and $Ti_{1-x}Al_xN$ ($\varepsilon_{0.5} = 2.2\%$) can be understood, see figures 6(*a*) and (*b*), where a considerably larger lattice strain for $Sc_{1-x}Al_xN$ is compensated by stronger electronic effects connected with populated nonbonding states for $Ti_{1-x}Al_xN$, see above.

Consequently, although electronic effects, related to the localization of d states at TM sites, obviously represent a considerable contribution to the mixing enthalpies and hence the phase stabilities of cubic $TM_{1-x}Al_xN$, they certainly cannot exclusively explain an overall increasing stability with increasing TM VEC. Based on the results presented, the phase stabilities of cubic $TM_{1-x}Al_xN$ need to be discussed in the context of size and electronic effects together. This is consistent with the experimental data obtained here, see section 4.1 on structural and thermal analysis. This is furthermore in line with results by Alling *et al* [38].

Our experimental investigations indicate that the maximum Al content for single phase cubic $TM_{1-x}Al_xN$ increases from $x = 0.48 \pm 0.02$ to 0.54 ± 0.02 to 0.68 ± 0.02 for TM = Ti, V and Cr, respectively. Also the onset temperature for the formation of hcp-AlN increases from temperatures slightly below 900 °C to ~900 °C to ~1200 °C for TM = Ti, V and Cr, respectively. This is in agreement with a decrease in the driving force for decomposition from $\Delta H_m \approx 0.1$ to 0.05 to 0.03 eV/atom at $x = 0.5$. It is furthermore consistent with decreasing $\varepsilon_{0.5}$ from 2.2 to 0.6 to 0.8% for TM = Ti, V and Cr, respectively. As discussed above, the somewhat smaller strain for $V_{1-x}Al_xN$ as compared with $Cr_{1-x}Al_xN$ is overcompensated by the larger electronic driving force for decomposition, i.e. a larger DOS at E_F, for $V_{1-x}Al_xN$. When, however, the lattice parameter difference between the binary constituents causes a lattice strain that exceeds a certain threshold, which based on the data obtained here is ~5%

Table 2. The local DOS at E_F for relaxed cubic $TM_{1-x}Al_xN$ (TM = Sc, Ti, V, Cr, Y, Zr and Nb) supercells, where one TM is incorporated into a 32 atom fcc-AlN supercell.

TM	Sc	Ti	V	Cr	Y	Zr	Nb
TM-local DOS at E_F (states eV^{-1})	0	2.393	3.607	0	0	1.488	3.073

(i.e. $Sc_{0.5}Al_{0.5}N$), the latter determines the phase stability of cubic $TM_{1-x}Al_xN$ overruling electronic structure related contributions.

The experimentally observed differential N release for different TMNs suggests that N loss and also off stoichiometry may significantly affect the phase stability of $TM_{1-x}Al_xN$, which is consistent with the findings of Alling and co-workers [39]. It is envisioned that future stability models that include N loss and off stoichiometry *per se* will allow for accurate predictions of the phase stability of Al-containing TM nitrides.

5. Conclusions

Based on the results obtained here the phase stability of ternary metastable cubic $TM_{1-x}Al_xN$ (TM = Sc, Ti, V, Cr, Y, Zr, Nb) is controlled by the lattice strain due to lattice parameter differences between fcc-TMN and fcc-AlN together with electronic structure effects. Latter may become dominant only if the lattice strain is below ∼5%, whereas for larger values, the phase stability is mainly controlled by lattice strain.

Furthermore, the experimentally observed indications for spinodal decomposition of cubic $Ti_{1-x}Al_xN$ which are not observed for cubic $V_{1-x}Al_xN$ and $Cr_{1-x}Al_xN$, may be understood based on the data presented. First, $Ti_{1-x}Al_xN$ exhibits the highest tendency for decomposition, mainly associated with the highest lattice strain of the experimentally investigated $TM_{1-x}Al_xN$ and secondly, the stable binary constituents fcc-TiN and hcp-AlN are only mildly affected by N loss. The enhanced N loss observed for $V_{1-x}Al_xN$ and $Cr_{1-x}Al_xN$ is consequently related to the lower stabilities of fcc-VN and fcc-CrN, which are both subject to decomposition induced N loss. The early N loss together with the lower mixing enthalpies of $V_{1-x}Al_xN$ and $Cr_{1-x}Al_xN$ may furthermore promote decomposition by nucleation and growth processes rather than spinodal decomposition. Hence, it may be speculated that these systems directly precipitate hcp-AlN without the intermediate formation of cubic Al-rich domains because the onset of decomposition due to low mixing enthalpies occurs at temperatures when pronounced N loss compensates the nucleation retarding volume mismatch between hcp-AlN and the cubic $TM_{1-x}Al_xN$ (TM = V, Cr) matrix. Our data hence indicate that in addition to the decomposition energetics (cubic $TM_{1-x}Al_xN \rightarrow$ cubic TMN + hexagonal AlN) future stability models have to include nitrogen release as one of the mechanisms that critically determine the overall phase stability of $TM_{1-x}Al_xN$.

Acknowledgment

Financial support from the START programme (Y371) of the Austrian Science Fund (FWF) is highly acknowledged by PHM. JMS gratefully acknowledges the financial support granted by Deutsche Forschungsgemeinschaft (DFG) within the project Schn. 735/14.

References

[1] Knotek O, Bohmer M and Leyendecker T 1986 *J. Vac. Sci. Technol. A: Vac. Surf. Films* **4** 2695
[2] Knotek O and Leyendecker T 1987 *J. Solid State Chem.* **70** 318
[3] Knotek O, Loffler F and Scholl H J 1991 *Surf. Coat. Technol.* **45** 53
[4] Münz W-D 1986 *J. Vac. Sci. Technol. A: Vac. Surf. Films* **4** 2717
[5] Münz W D and Gobel J 1987 *Surf. Eng.* **3** 47
[6] PalDey S and Deevi S C 2003 *Mater. Sci. Eng.* A **342** 58
[7] Endrino J L, Fox-Rabinovich G S and Gey C 2006 *Surf. Coat. Technol.* **200** 6840
[8] Kalss W, Reiter A, Derflinger V, Gey C and Endrino J L 2006 *Int. J. Refract. Met. Hard Mater.* **24** 399
[9] Reiter A E, Brunner B, Ante M and Rechberger J 2006 *Surf. Coat. Technol.* **200** 5532
[10] Reiter A E, Derflinger V H, Hanselmann B, Bachmann T and Sartory B 2005 *Surf. Coat. Technol.* **200** 2114
[11] Vetter J 1995 *Surf. Coat. Technol.* **76–77** 719
[12] Bobzin K, Lugscheider E, Maes M, Gold P W, Loos J and Kuhn M 2004 *Surf. Coat. Technol.* **188–189** 649
[13] Bobzin K, Lugscheider E, Nickel R and Immich P 2006 *Materialwiss. Werkstofftech.* **37** 833
[14] Lee S and Lee S 2006 *Diffus. Defect Data B: Solid State Phenom.* **116–117** 84
[15] Rodríguez-Baracaldo R, Benito J A, Puchi-Cabrera E S and Staia M H 2007 *Wear* **262** 380
[16] Spain E, Avelar-Batista J C, Letch M, Housden J and Lerga B 2005 *Surf. Coat. Technol.* **200** 1507
[17] Yang S G, Pakhomov A B, Hung S T and Wong C Y 2002 *Appl. Phys. Lett.* **81** 2418
[18] Cremer R, Witthaut M and Neuschütz D 1998 Experimental determination of the metastable (Ti,Al)N phase diagram up to 700 °C *Value-Addition Metallurgy* ed Cho W D and Sohn H Y (Warrendale, PA: The Minerals and Metals Society) p 249
[19] Hörling A, Hultman L, Oden M, Sjolen J and Karlsson L 2002 *J. Vac. Sci. Technol. A: Vac. Surf. Films* **20** 1815
[20] Kimura A, Kawate M, Hasegawa H and Suzuki T 2003 *Surf. Coat. Technol.* **169–170** 367
[21] Kutschej K, Mayrhofer P H, Kathrein M, Polcik P, Tessadri R and Mitterer C 2005 *Surf. Coat. Technol.* **200** 2358
[22] Mayrhofer P H, Hörling A, Karlsson L, Sjölén J, Larsson T, Mitterer C and Hultman L 2003 *Appl. Phys. Lett.* **83** 2049
[23] Prange R, Cremer R and Neuschütz D 2000 *Surf. Coat. Technol.* **133–134** 208
[24] Rauch J Y, Rousselot C and Martin N 2002 *Surf. Coat. Technol.* **157** 138
[25] Kaindl R, Franz R, Soldan J, Reiter A, Polcik P, Mitterer C, Sartory B, Tessadri R and O'Sullivan M 2006 *Thin Solid Films* **515** 2197
[26] Kawate M 2002 *J. Vac. Sci. Technol.* A **20** 569
[27] Makino Y and Nogi K 1998 *Surf. Coat. Technol.* **98** 1008
[28] Sugishima A, Kajioka H and Makino Y 1997 *Surf. Coat. Technol.* **97** 590

[29] Hasegawa H, Kawate M and Suzuki T 2005 *Surf. Coat. Technol.* **200** 2409
[30] Makino Y, Mori M, Miyake S, Saito K and Asami K 2005 *Surf. Coat. Technol.* **193** 219
[31] Sanjinés R, Sandu C S, Lamni R and Lévy F 2006 *Surf. Coat. Technol.* **200** 6308
[32] Selinder T I, Miller D J, Gray K E, Sardela M R, Hultman L 1995 *Vacuum* **46** 1401
[33] Moser M, Mayrhofer P H, Kiener D and Scheu C 2009 *Surf. Coat. Technol.* submitted
[34] Mayrhofer P H, Willmann H, Hultman L and Mitterer C 2008 *J. Phys. D: Appl. Phys.* **41** 155316
[35] Mayrhofer P H, Willmann H and Reiter A E 2008 *Surf. Coat. Technol.* **202** 4935
[36] Rovere F and Mayrhofer P H 2008 *J. Vac. Sci. Technol. A: Vac. Surf. Films* **26** 29
[37] Willmann H, Mayrhofer P H, Persson P O A, Reiter A E, Hultman L and Mitterer C 2006 *Scr. Mater.* **54** 1847
[38] Alling B, Karimi A and Abrikosov I A 2008 *Surf. Coat. Technol.* **203** 883
[39] Alling B, Karimi A, Hultman L and Abrikosov I A 2008 *Appl. Phys. Lett.* **92** 071903
[40] Alling B, Marten T, Abrikosov I A and Karimi A 2007 *J. Appl. Phys.* **102** 044314
[41] Alling B, Ruban A V, Karimi A, Peil O E, Simak S I, Hultman L and Abrikosov I A 2007 *Phys. Rev.* B **75** 045123
[42] Hugosson H W, Hogberg H, Algren M, Rodmar M and Selinder T I 2003 *J. Appl. Phys.* **93** 4505
[43] Mayrhofer P H, Fischer F D, Böhm H J, Mitterer C and Schneider J M 2007 *Acta Mater.* **55** 1441
[44] Mayrhofer P H, Hultman L, Schneider J M, Staron P and Clemens H 2007 *Int. J. Mater. Res.* **11** 1054
[45] Mayrhofer P H, Music D, Reeswinkel T, Fuß H G and Schneider J M 2008 *Acta Mater.* **56** 2469
[46] Mayrhofer P H, Music D and Schneider J M 2006 *J. Appl. Phys.* **100** 094906
[47] Makino Y 2005 *Surf. Coat. Technol.* **193** 185
[48] Sheng S H, Zhang R F and Veprek S 2008 *Acta Mater.* **56** 968
[49] Zhang R F and Veprek S 2007 *Acta Mater.* **55** 4615
[50] *Powder Diffraction File* (card 65-0565 for fcc-TiN, card 25-1495 for fcc-AlN, card 25-1133 for hcp-AlN, card 35-0768 for fcc-VN, card 71-1139 for fcc-$VN_{.81}$, card 33-1439 for hcp-V_2N, card 65-2899 for fcc-CrN, card 35-0803 for hcp-Cr_2N, card 45-0978 for fcc-ScN, card 35-0779 for fcc-YN, card 35-0753 for fcc-ZrN, card 88-2404 for fcc-NbN)
[51] Hohenberg P and Kohn W 1964 *Phys. Rev.* **136** B864
[52] Kresse G and Hafner J 1993 *Phys. Rev.* B **48** 13115
[53] Kresse G and Hafner J 1994 *Phys. Rev.* B **49** 14251
[54] Kresse G and Joubert D 1999 *Phys. Rev.* B **59** 1758
[55] Blöchl P E 1994 *Phys. Rev.* B **50** 17953
[56] Monkhorst H J and Pack J D 1976 *Phys. Rev.* B **13** 5188
[57] Zunger A, Wei S H, Ferreira L G and Bernard J E 1990 *Phys. Rev. Lett.* **65** 353
[58] Abrikosov I A, Niklasson A M N, Simak S I, Johansson B, Ruban A V and Skriver H L 1996 *Phys. Rev. Lett.* **76** 4203
[59] Abrikosov I A, Simak S I, Johansson B, Ruban A V and Skriver H L 1997 *Phys. Rev.* B **56** 9319
[60] Cowley J M 1950 *J. Appl. Phys.* **21** 24
[61] Keijser T H 1981 *J. Appl. Crystallogr.* **15** 308
[62] Massalski T B 1990 *Binary Alloy Phase Diagrams* (Metals Park: ASM International)
[63] Okamoto H 1994 *J. Phase Equilib. Diffus.* **15** 454
[64] Mayrhofer P H, Mitterer C, Hultman L and Clemens H 2006 *Prog. Mater. Sci.* **51** 1032
[65] Adibi F, Petrov I, Hultman L, Wahlstrom U, Shimizu T, McIntyre D, Greene J E and Sundgren J E 1991 *J. Appl. Phys.* **69** 6437
[66] Cahn J W 1961 *Acta Metall.* **9** 795
[67] Rovere F, Mayrhofer P H, Reinholdt A, Mayer J and Schneider J M 2008 *Surf. Coat. Technol.* **202** 5870
[68] Ohtani H and Hillert M 1991 *CALPHAD* **15** 11
[69] Qi W H and Wang M P 2004 *Mater. Chem. Phys.* **88** 280
[70] Predel B 1991 *Landolt-Börnstein—Group IV Physical Chemistry*, vol 5a: Ac Au–Au-Zr (Berlin: Springer)
[71] Predel B 1997 *Landolt-Börnstein—Group IV Physical Chemistry*, vol 5H: Li Mg–Nd-Zr (Berlin: Springer)
[72] Predel B 1994 *Landolt-Bornstein—Group IV Physical Chemistry*, vol 5d: Cr Cs–Cu-Zr (Berlin: Springer)
[73] Häglund J, Fernández Guillermet A, Grimvall G and Körling M 1993 *Phys. Rev.* B **48** 11685
[74] Fernández Guillermet A, Häglund J and Grimvall G 1992 *Phys. Rev.* B **45** 11557
[75] Schwarz K 1987 *Crit. Rev. Solid State Mater. Sci.* **13** 211
[76] Corliss L M, Elliott N and Hastings J M 1960 *Phys. Rev.* **117** 929
[77] Filippetti A, Pickett W E and Klein B M 1999 *Phys. Rev.* B **59** 7043
[78] Ibberson R M and Cywinski R 1992 *Physica B: Condens. Matter* **180–181** 329
[79] Smirnova E A, Korzhavyi P A, Vekilov Y K, Johansson B and Abrikosov I A 2002 *Eur. Phys. J. B—Condens. Matter Complex Syst.* **30** 57
[80] Hollec D, Franz R, Mayrhofer P H and Mitterer C 2009 *J. Appl. Phys.* submitted
[81] Vegard L 1921 *Z. Phys.* **5** 17
[82] Jacob K T, Raj S and Rannesh L 2007 *Int. J. Mater. Res.* **98** 776